Overcharge Protection in Aqueous Zinc-Ion Batteries via Self-Sacrificial Additives

Shuo Yang[a], Liang Mei[a], Zhuoxi Wu[a], Jiaxiong Zhu[a], Pei Li[a], Hu Hong[a], Zhiyuan Zeng[a], Hongfei Li[d] *, Funian Mo[c] *, Chunyi Zhi[a, b]*

[a] Department of Materials Science and Engineering, City University of Hong Kong, 83 Tat Chee Avenue, Hong Kong, China

[b] Center for Advanced Nuclear Safety and Sustainable Development, City University of Hong Kong, Kowloon, Hong Kong, 999077, China

[c] School of Future Technology, Shenzhen Technology University, Shenzhen, 518055, China.

[d] School of System Design and Intelligent Manufacturing, Southern University of Science and Technology, Shenzhen, Guangdong, 518055, China

* Email address: lihf@sustech.edu.cn; mofunian@sztu.edu.cn; cy.zhi@cityu.edu.hk

Keywords: zinc batteries, aqueous batteries, overcharge protection, redox-active additives

Methods

Chemicals: H_2O_2 (30%) was purchased from Fisher Chemical, and hydrazine hydrate (50%) was purchased from Acros Organics. V_2O_5 (99%), Manganese sulfate tetrahydrate ($MnSO_4 \cdot 4H_2O$, 99%), Manganese acetate ($Mn(AC)_2$, 98%), ethanol (99.8%), NaClO solution (6-14% active chlorine basis), zinc sulfate heptahydrate ($ZnSO_4 \cdot 7H_2O$, AR), zinc trifluoromethanesulfonate (ZnOTF, 98%), tetrabutylammonium bromide (TBABr, 99%) and benzyltrimethylammonium bromide (BTABr, 98%) were purchased from Aladdin reagent. All the chemicals were used as received without further purification. The deionized water (DI water) was purified on a MilliQ device from Millipore.

Preparation of cathode.

Mn^{2+} expanded hydrated V_2O_5 (MnVO) cathode material with a micro-flower-like shape was prepared according to a previous study.[1] Specifically, we dissolved 2 mmol of V_2O_5 in a mixture of 50 mL H_2O and 2 mL H_2O_2, and separately dissolved 1 mmol of $MnSO_4 \cdot 4H_2O$ in 30 mL H_2O. The two solutions were then admixed and transferred to a 100 Teflon lined stainless steel autoclave, which was heated to and held at 120 ℃ for 6 h. Afterward, brick red precipitates were collected by centrifugation and washed three times with water and ethanol. Finally, the collected precipitates were dried at 70 ℃ overnight.

The synthesis of MnO_2 was conducted following previous work in our research group, with slight modifications.[2] Initially, 3 ml of hydrazine hydrate solution was introduced into a 40 mL $Mn(Ac)_2$ solution with a concentration of 4 mmol L^{-1},

followed by 5 minutes of stirring. Subsequently, the solution was transferred to a 100 mL Teflon-lined stainless-steel autoclave and subjected to hydrothermal treatment at 180 °C for 12 hours. The $Mn(OH)_2$ was obtained by centrifugation and then freeze-dried at 60 °C under vacuum. After that, 0.2 g of $Mn(OH)_2$ was dispersed in 50 ml of water containing 10 mL of NaClO solution and reacted for 24 hours under stirring. The final MnO_2 nanoplates were collected after washing the black suspension and dried under a vacuum at 60 °C overnight.

To prepare the cathode, a slurry containing the active material, Ketjenblack, and poly(1,1-difluoroethylene) (PVDF) in a weight ratio of 70:20:10 was coated onto a carbon cloth, which was then dried under vacuum at 60 °C for 12 hours.

Electrochemical Characterizations.

All the batteries were assembled into CR-2032 coin cells (full cell), where bare 100 μm Zn served as the anode, and a glass fiber separator (Waterman-1820, 675) was utilized. For Zn||MnVO batteries, the electrolyte employed was 3 M zinc trifluoromethanesulfonate (ZnOTF). In order to protect the batteries from overcharging, TBABr was included in the electrolyte at a concentration of 0.4 mol L^{-1}. For Zn||MnO_2 batteries, the electrolyte consisted of 2 M $ZnSO_4$ and 0.2 M $MnSO_4$. BTABr was added to the electrolyte at a concentration of 0.1 mol L^{-1} to provide overcharge protection. The amount of electrolyte used in the batteries was about 150 μL.

The galvanostatic charging-discharging processes were conducted using the Land battery testing system (Wuhan, China) at different current densities under ambient

temperature. All the batteries were cycled at a current density of 0.5 A g^{-1}. In order to test the electrochemical performance under overcharging conditions, the batteries were first charged until reaching a specified capacity and then discharged to certain voltages. The calculation of specific capacity was based on the mass loading of active materials, which was about 1-3 mg cm^{-2}.

The cyclic voltammogram (CV) and electrochemical impedance spectroscopy (EIS) measurements were conducted using a CHI-760 electrochemical working station.

Characterizations.

The crystal structure and phase composition were characterized by X-ray diffraction (XRD) using a Rigaku X-ray Diffractometer SmartLabTM 9kW (Cu Kα, λ = 0.154 nm). The micromorphology of products was investigated by scanning electron microscope (SEM, ESEM, FEI/Philips XL30). The X-ray Photoelectron Spectrometer (XPS) studies were performed using a PHI5000 VersaProbe II photoelectron spectrometer, and the spectra were calibrated using a carbon spectrum as a reference. An inductively coupled plasma-optical emission spectrometer (ICP-OES, Agilent ICPOES730) was used to monitor the evolution of electrolyte ions. The pH evolution of the electrolyte was monitored using a pH meter in batteries assembled in polystyrene cuvettes (10 × 10 × 45 mm) commonly used for UV-Vis spectroscopy measurements. The *operando* gas pressure measurement was performed using a gas pressure sensor connected to a sealed electrochemical cell. Before the tests, the cell was filled with Ar gas to replace the air. Based on the ideal gas law, the gas pressure (in kPa) was converted to the gas amount (in nmol). The *in-situ* GC measurement

was performed on a gas chromatography system (GC 2060, Shanghai Ruimin Instruments Co., Ltd.) connected to a sealed electrochemical cell.

Computational details.

The electrostatic potential (ESP) calculation was conducted using the DMol3 package. The structure optimization and calculations were described using the B3LYP hybrid functional, and the Grimme method was used for dispersion-corrected density functional theory calculations (DFT-D). DFT semicore pseudopotential core treatment was implemented for relativistic effects, replacing core electrons with a single effective potential. Double numerical plus polarization was employed as the basis set. The convergence tolerance of energy of 10^{-6} Hartree was taken (1 Hartree = 27.21 eV), and the maximal allowed force and displacement were 0.002 and 0.005 Hartree $Å^{-1}$, respectively.

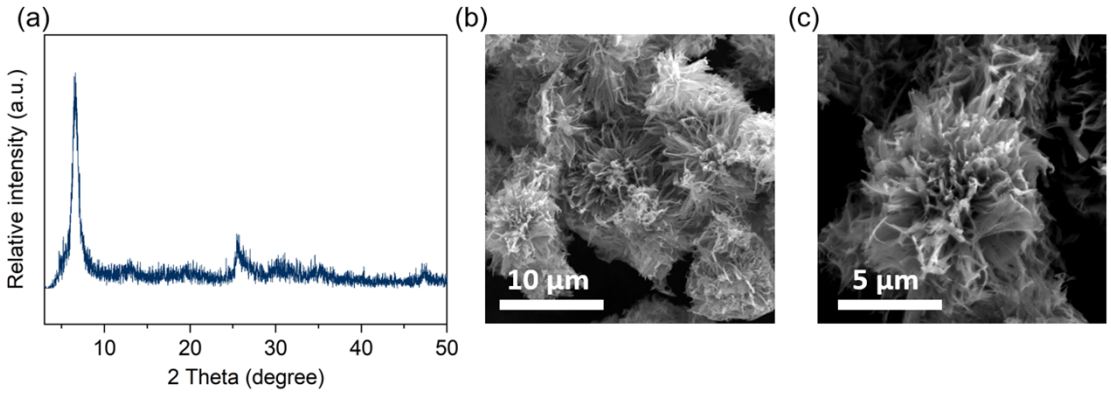

Figure S1. (a) XRD pattern of the as-prepared MnVO. The Miller indices corresponding to the crystallographic planes are not currently available in the database. However, the diffraction peaks are consistent with the previous report.[1] (b) and (c) SEM images of MnVO showing the aggregation of nanosheets into a micro-flower-like morphology.

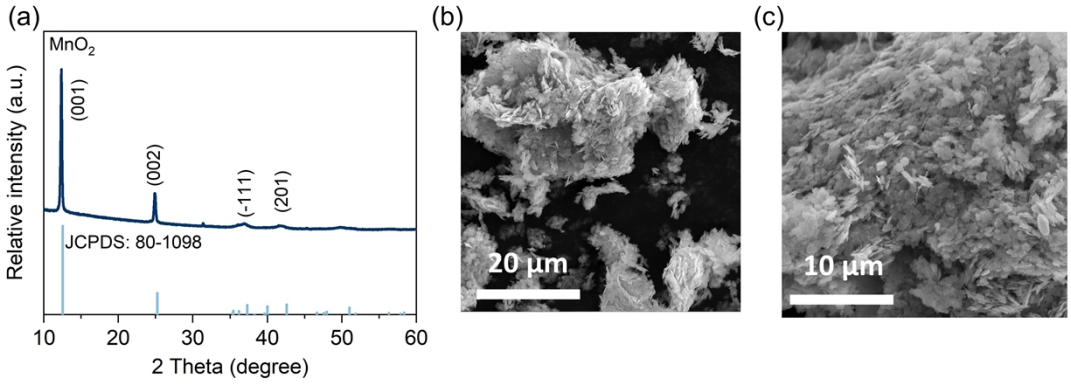

Figure S2. (a) XRD pattern, (b) and (c) SEM images exhibiting an irregular hexagonal nanoplate morphology of the as-prepared MnO_2.

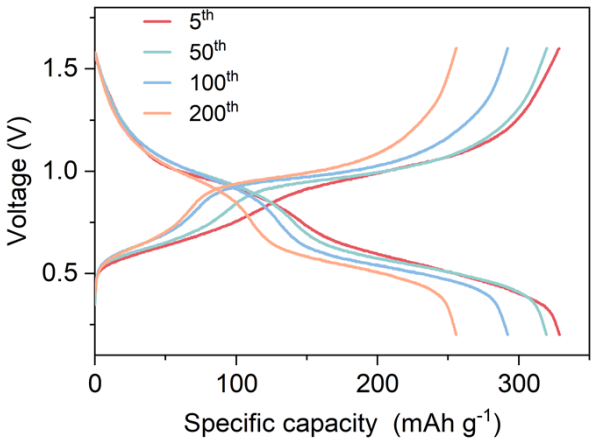

Figure S3. GCD curves of Zn||MnVO batteries cycling at normal operation.

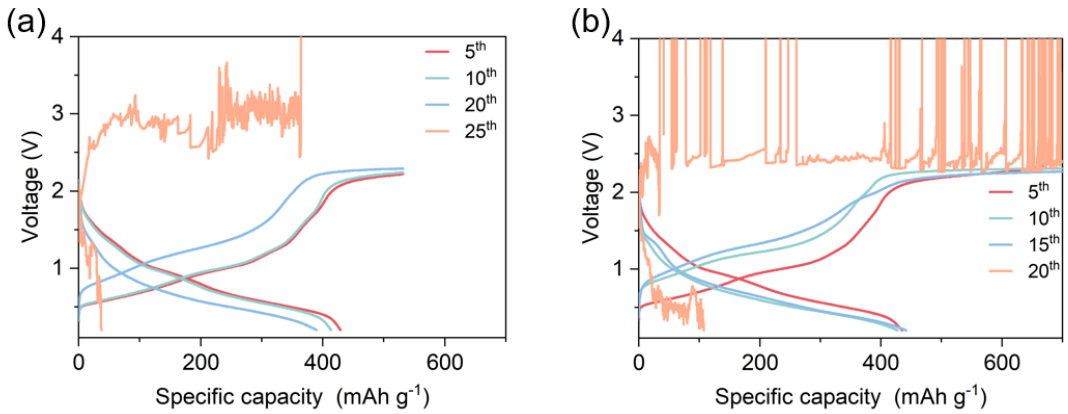

Figure S4. GCD curves of Zn||MnVO batteries cycling at (a) 150% SOC and (b) 200% SOC.

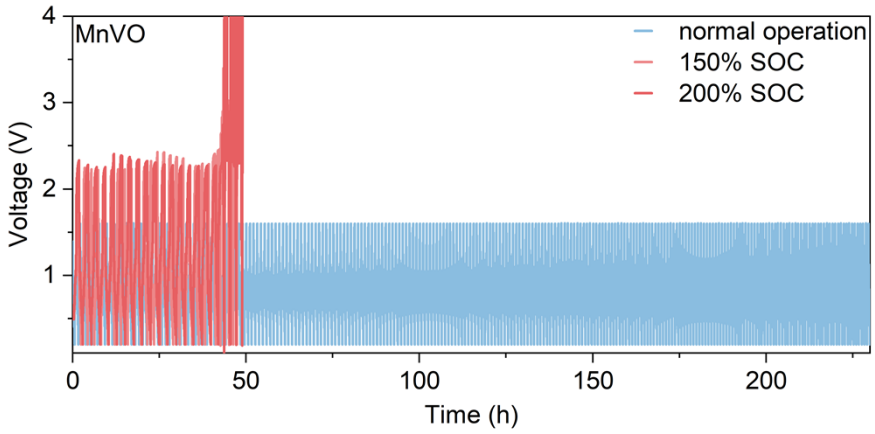

Figure S5. Voltage-time curves of Zn||MnVO batteries operating at different conditions.

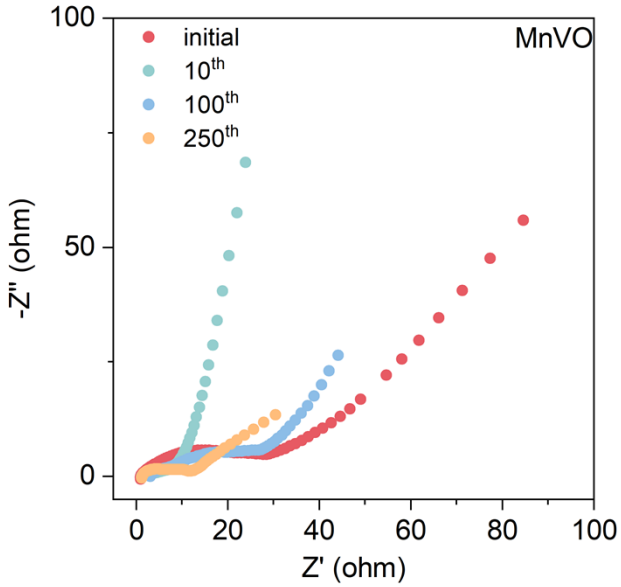

Figure S6. EIS curves of Zn||MnVO batteries cycling at normal operations.

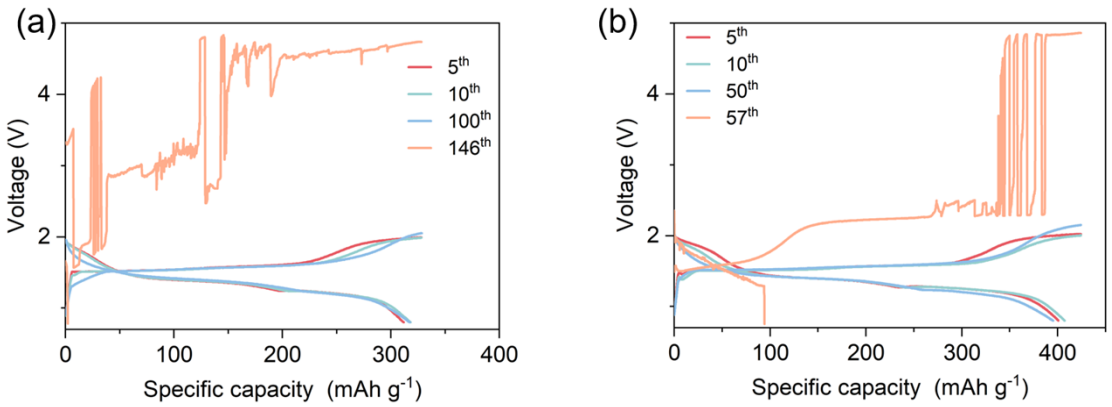

Figure S7. GCD curves of Zn||MnO_2 batteries cycling at (a) 150% SOC and (b) 200% SOC.

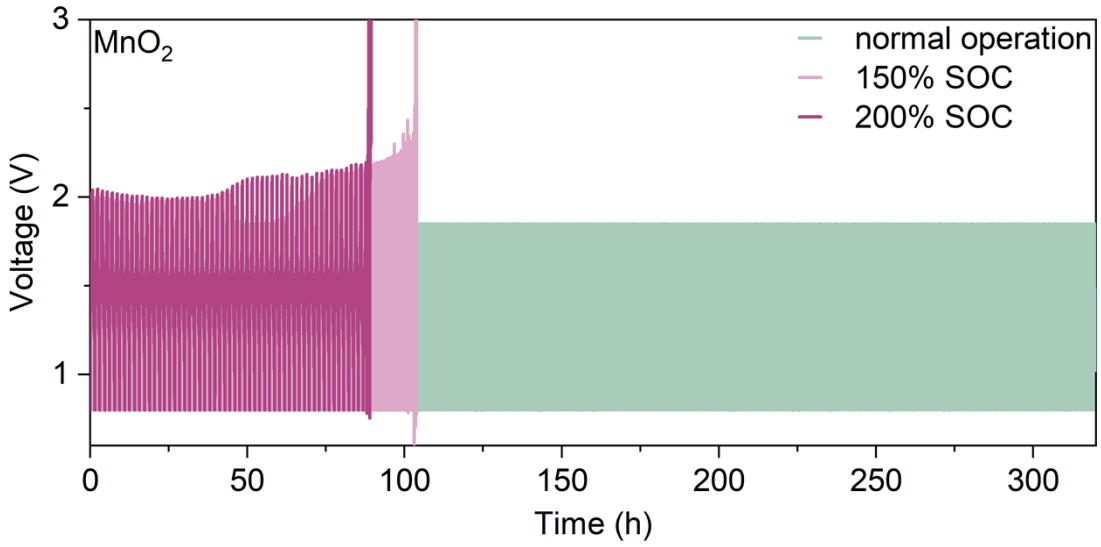

Figure S8. Voltage-time curves of Zn||MnO_2 batteries operating at different conditions.

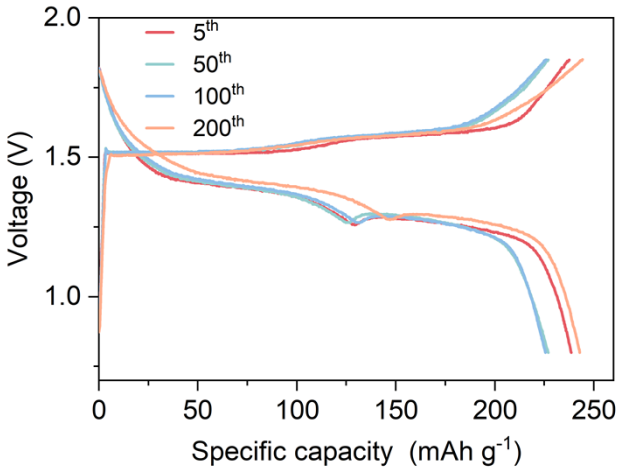

Figure S9. GCD curves of Zn||MnO_2 batteries cycling at normal operation.

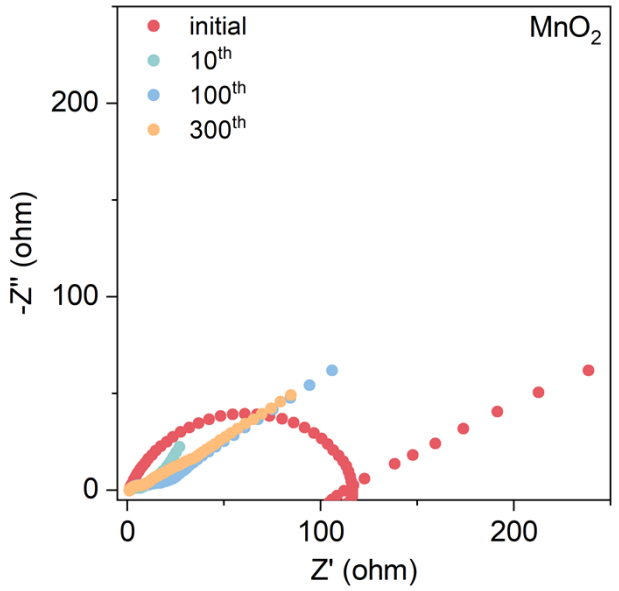

Figure S10. EIS curves of Zn||MnO_2 batteries cycling at normal operation.

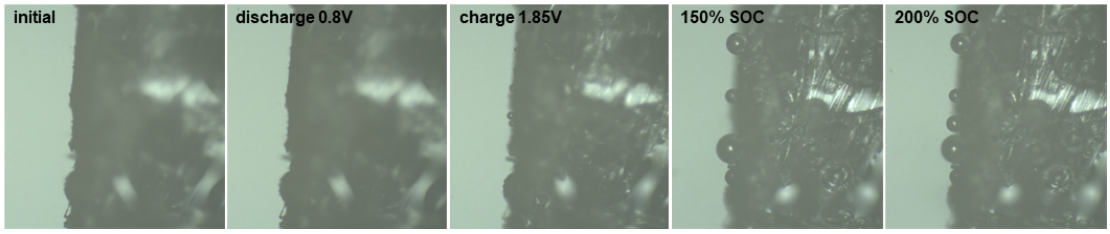

Figure S11. *In-situ* optical microscope images demonstrating the gas generation at the electrode surface.

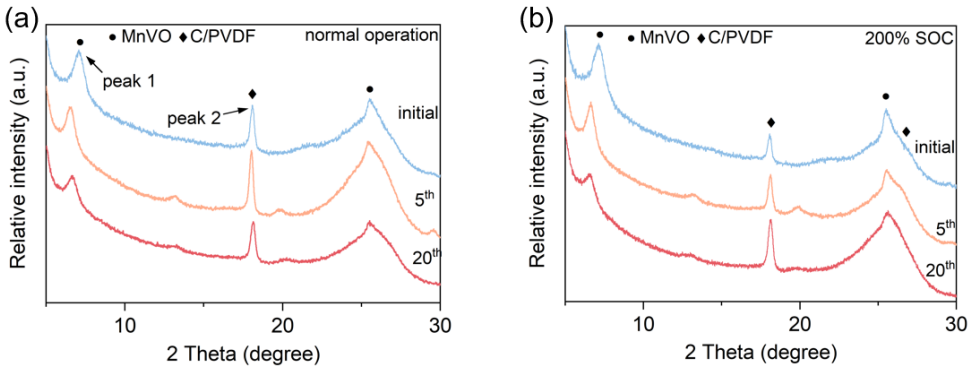

Figure S12. XRD pattern of MnVO electrode cycling at (a) normal operation and (b) 200% SOC.

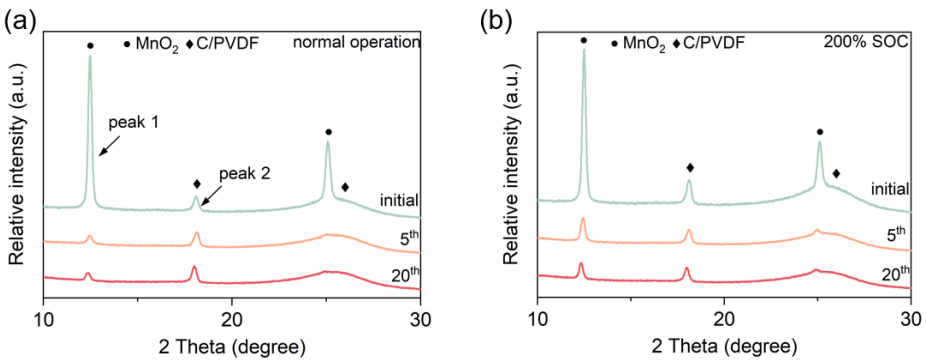

Figure S13. XRD pattern of MnO_2 electrode cycling at (a) normal operation and (b) 200% SOC

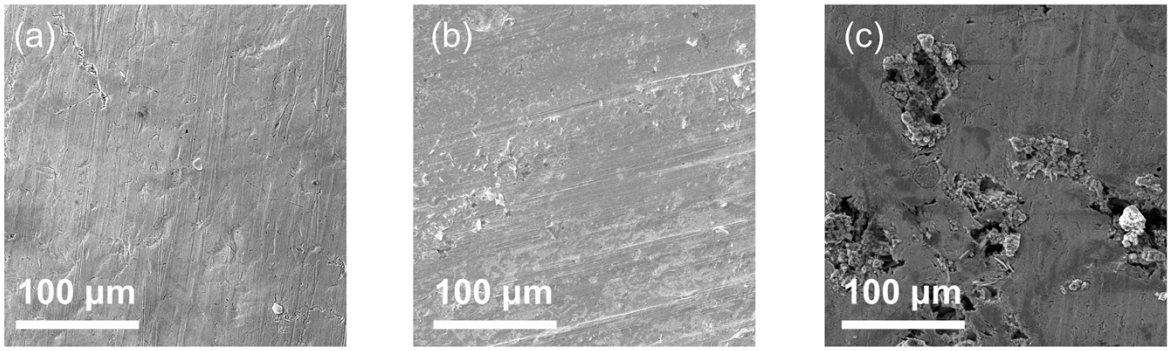

Figure S14. SEM images of Zn anode (a) at the initial state, after cycling at (h) normal operations and (i) 200% SOC for 10 cycles in Zn||MnO_2 batteries.

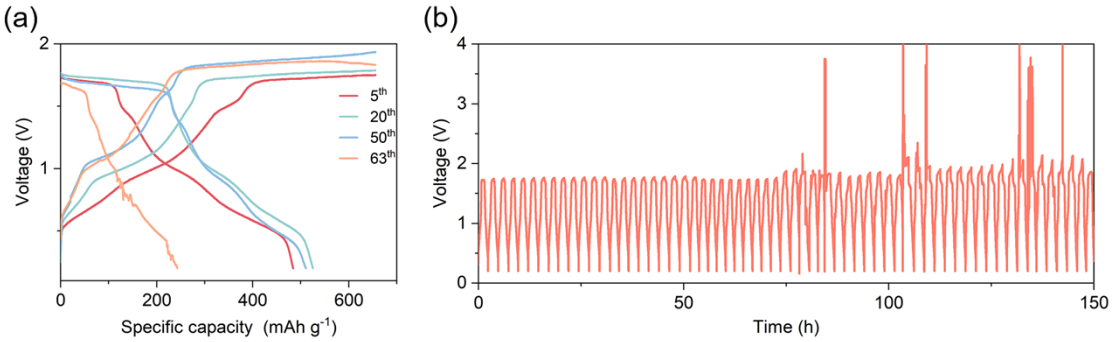

Figure S15. (a) Selective GCD and (b) voltage-time curves of Zn||MnVO batteries with BTABr additive in the electrolyte.

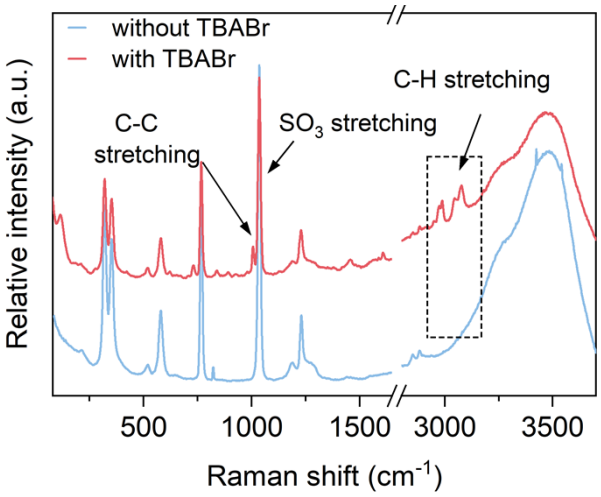

Figure S16.Raman spectra for electrolytes of Zn||MnVO batteries with and without TBABr additive.

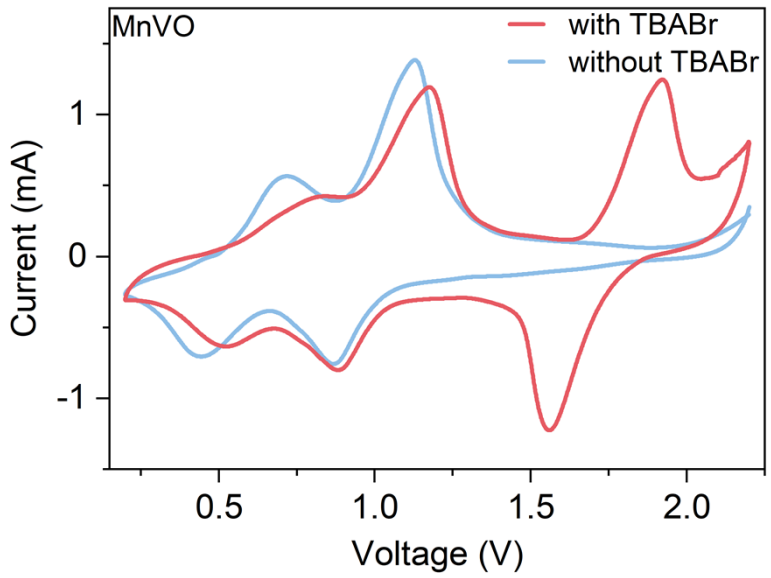

Figure S17. CV curves of Zn||MnVO batteries with and without TBABr additive at a scan rate of 2 mV s^{-1}.

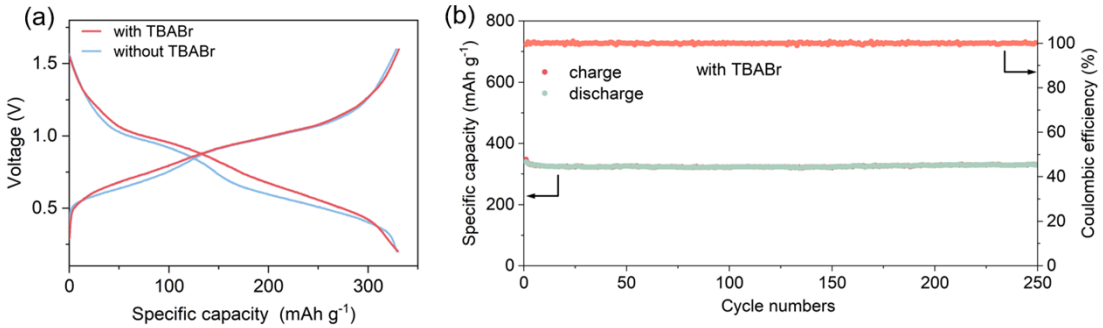

Figure S18. (a) GCD curves of Zn||MnVO batteries with and without TBABr additive at normal operation. (b) Cycling performance of Zn||MnVO batteries with TBABr additive at normal operation.

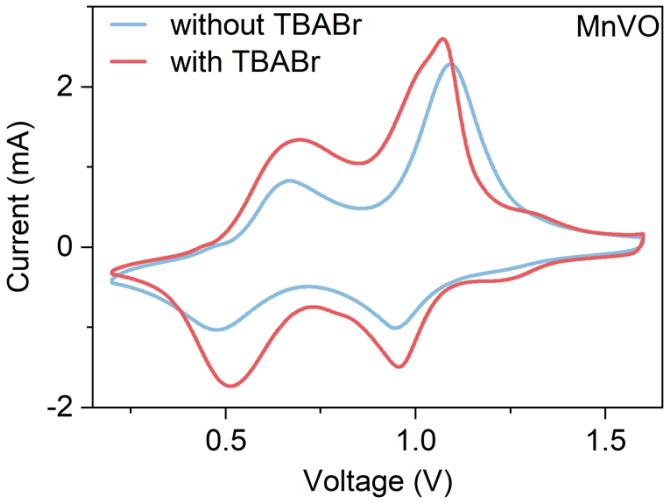

Figure S19. CV curves of Zn||MnVO batteries with and without TBABr additive at normal operation.

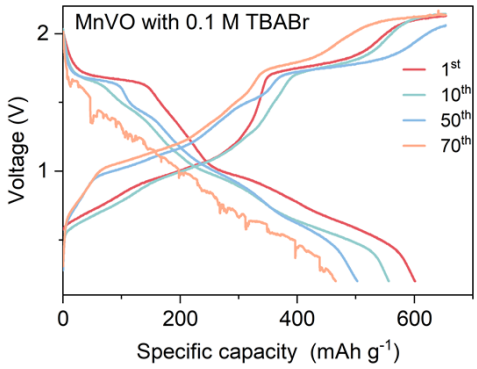

Figure S20. Selective GCD curves of Zn||MnVO batteries with a lower concentration of BTABr additive (0.1 M) in the electrolyte.

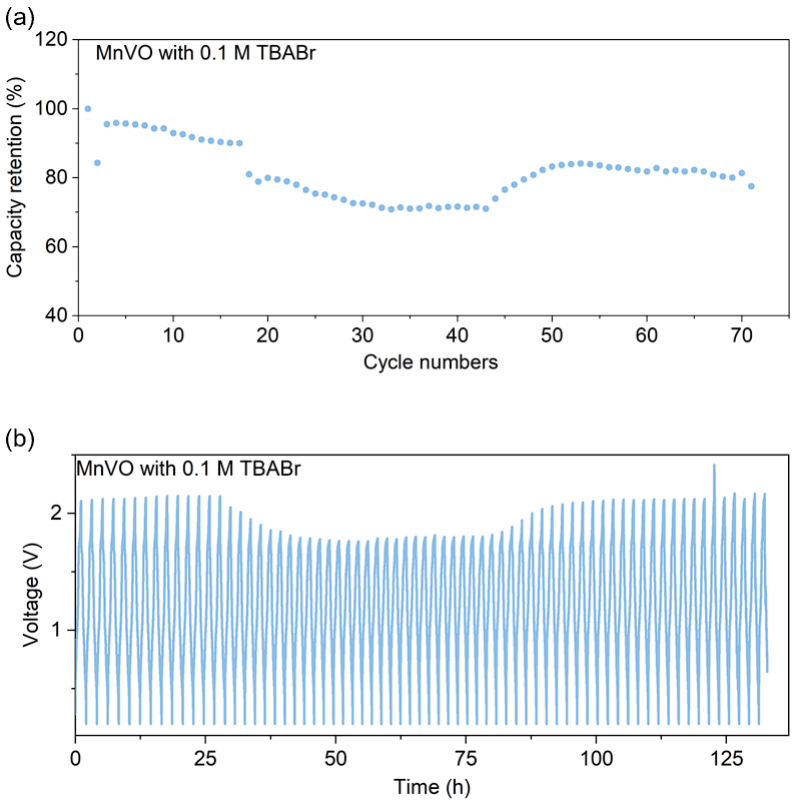

Figure S21. (a) Cycling performance of Zn||MnVO batteries with a lower concentration of TBABr additive (0.1 M) in the electrolyte operating at 200% SOC, and the corresponding (b) voltage-time curves.

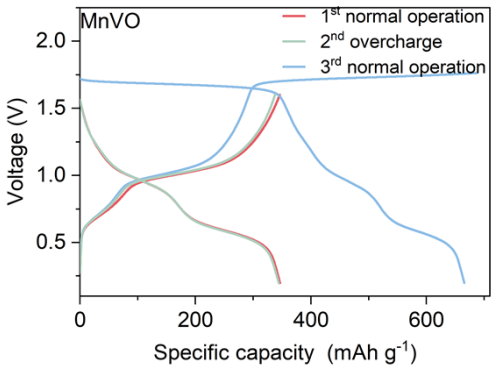

Figure S22. GCD curves of Zn||MnVO batteries with TBABr additive at normal operation, followed by overcharge conditions and subsequent recovery to normal operation.

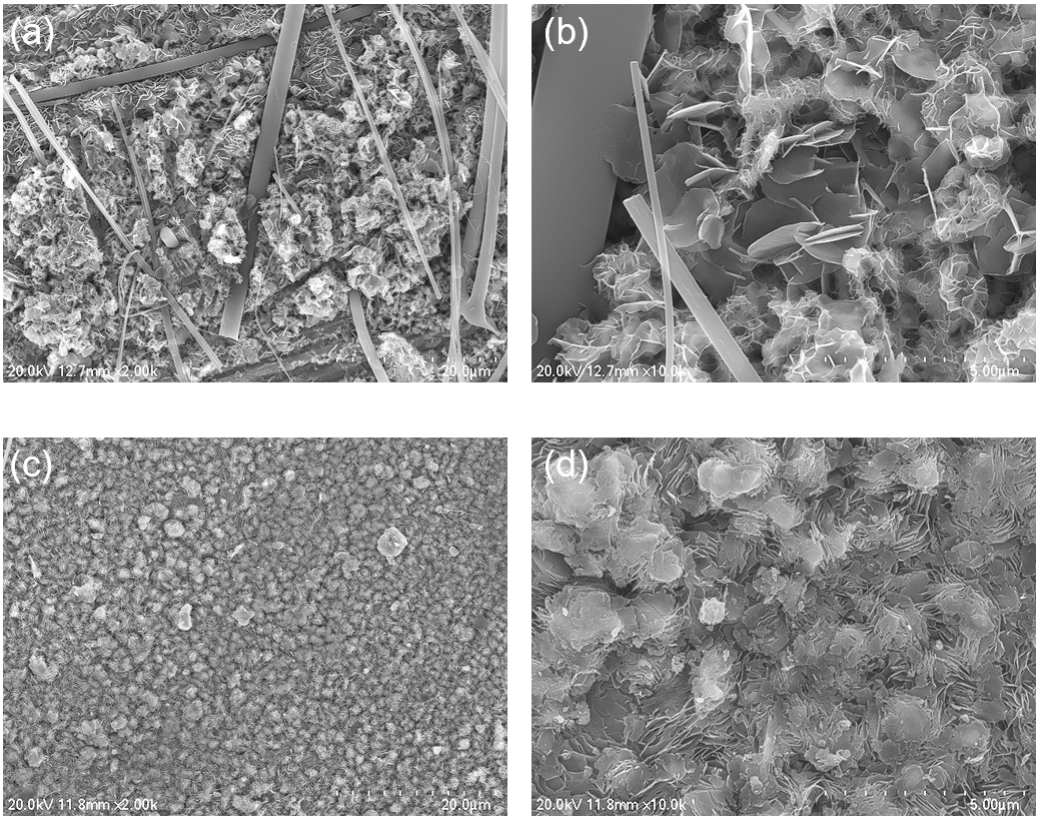

Figure S23. SEM images of Zn deposition in the electrolyte of Zn||MnVO batteries (a) and (b) without TBABr additive; (c) and (d) with TBABr additive.

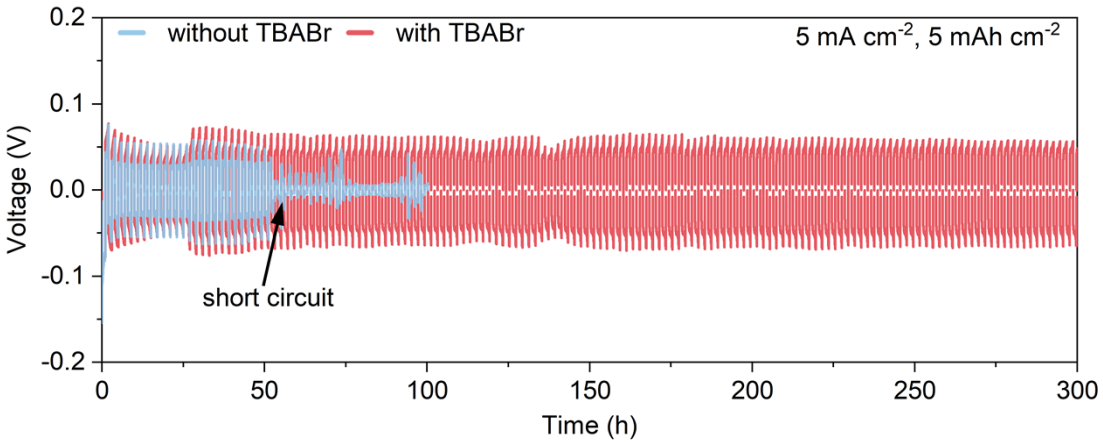

Figure S24. Voltage-time curves for Zn||Zn half-cells in electrolytes of Zn||MnVO batteries, comparing configurations with and without the TBABr additive.

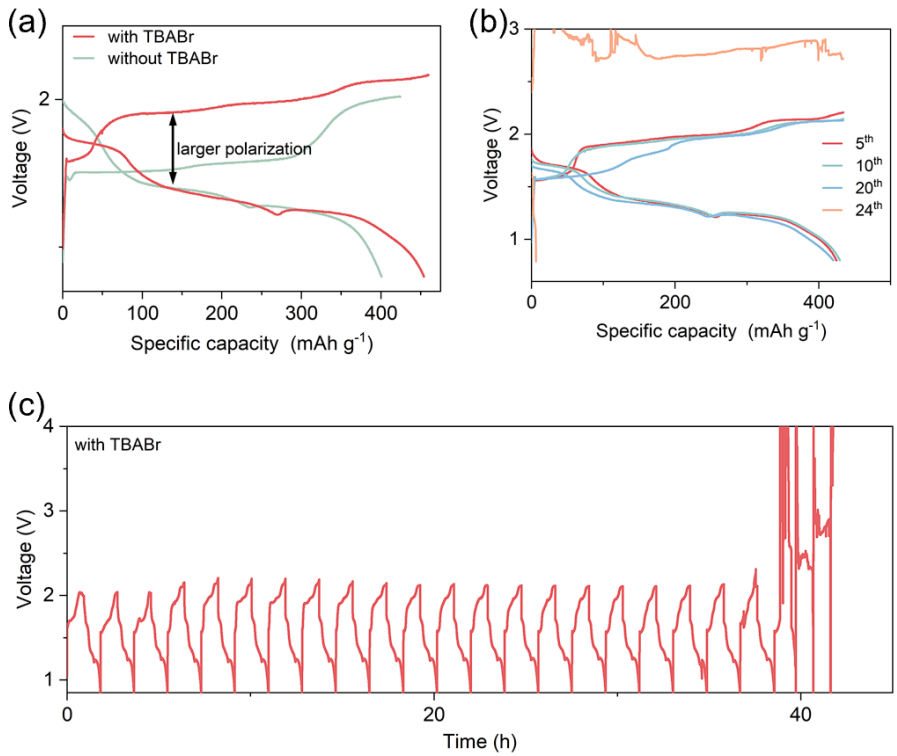

Figure S25. (a) GCD curves of Zn||MnO_2 batteries with and without TBABr additive at 200% SOC. (b) selected GCD and (c) voltage-time curves of Zn||MnO_2 batteries with TBABr additive cycling at 200% SOC.

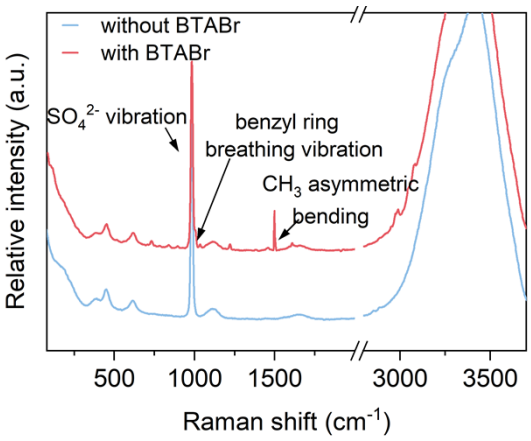

Figure S26.Raman spectra for electrolytes of Zn||MnO_2 batteries with and without BTABr additive.

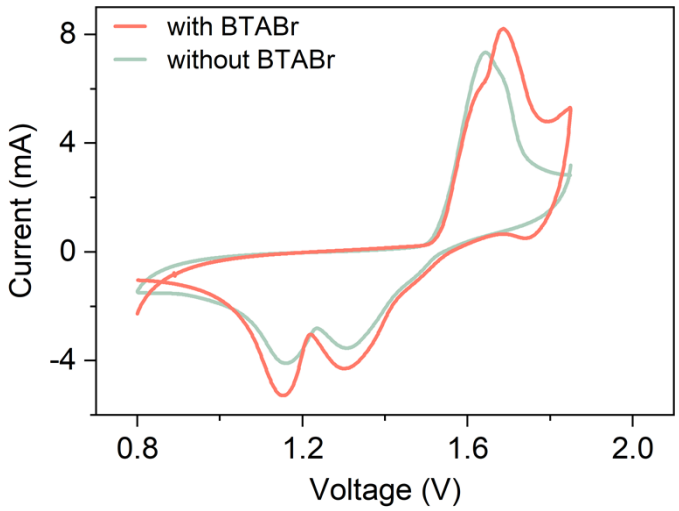

Figure S27. CV curves of Zn||MnO_2 batteries with and without BTABr additive at normal operation.

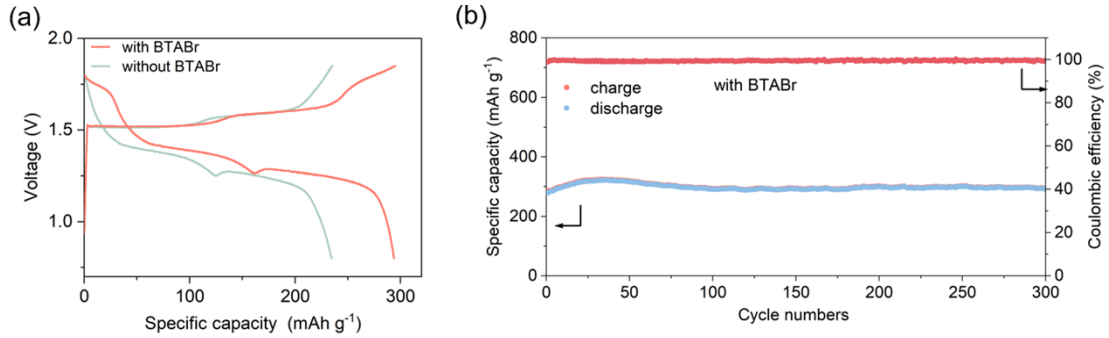

Figure S28. (a) GCD curves of Zn||MnO_2 batteries with and without BTABr additive at normal operation. (b) Cycling performance of Zn||MnO_2 batteries with BTABr additive at normal operation.

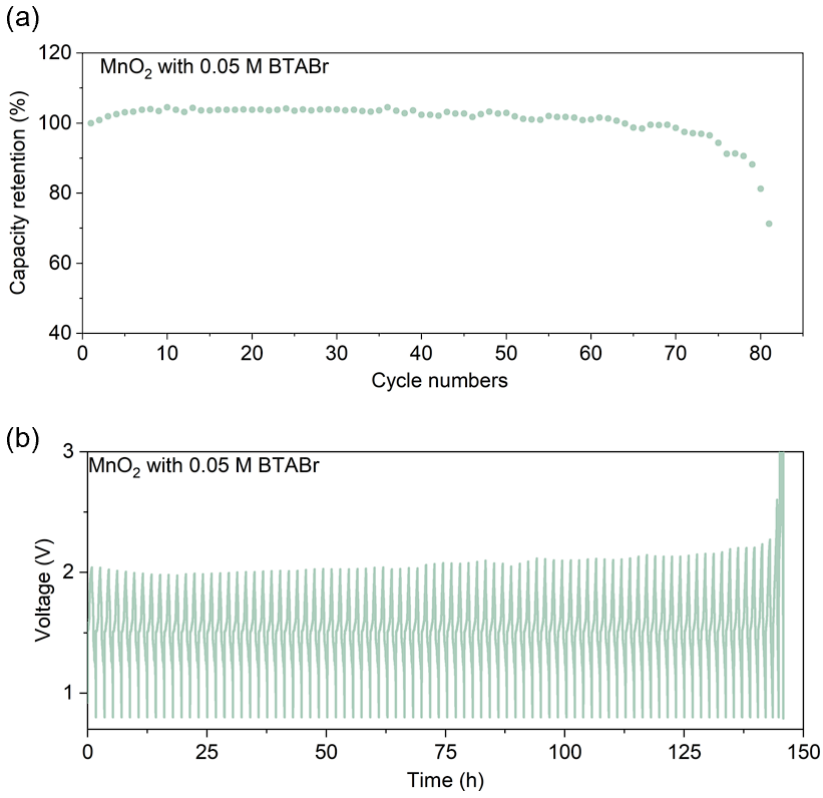

Figure S29. (a) Cycling performance of Zn||MnO_2 batteries with a lower concentration of BTABr additive (0.05 M) in the electrolyte operating at 200% SOC, and the corresponding (b) voltage-time curves.

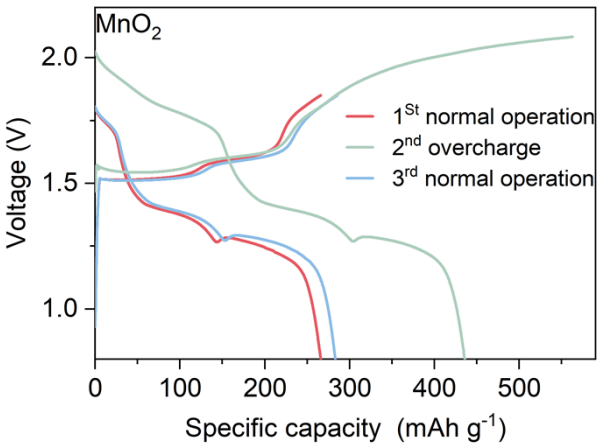

Figure S30. GCD curves of Zn||MnO_2 batteries with BTABr additive at normal operation, followed by overcharge conditions and subsequent recovery to normal operation.

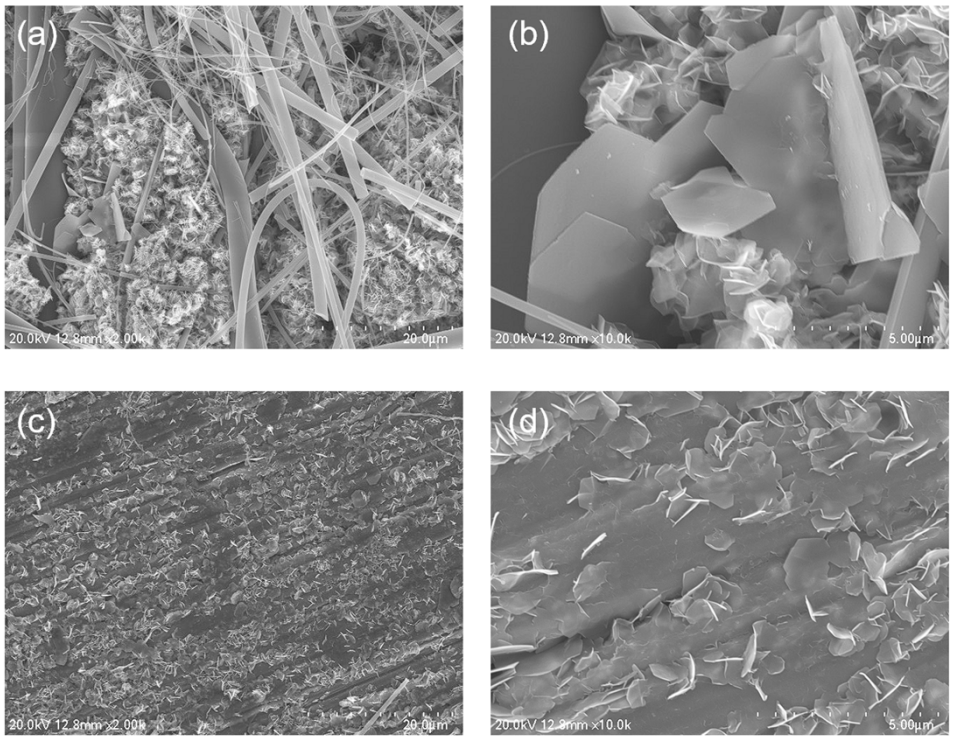

Figure S31. SEM images of Zn deposition in the electrolyte of Zn||MnO_2 batteries (a) and (b) without BTABr additive; (c) and (d) with BTABr additive.

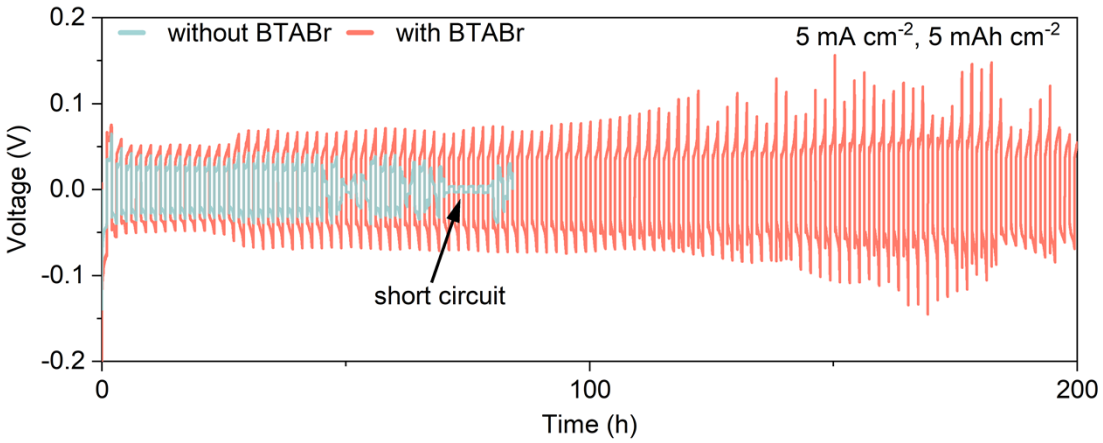

Figure S32. Voltage-time curves for Zn||Zn half-cells in electrolytes of Zn||MnO_2 batteries, comparing configurations with and without the BTABr additive.

References

1. Liu, C.; Neale, Z.; Zheng, J.; Jia, X.; Huang, J.; Yan, M.; Tian, M.; Wang, M.; Yang, J.; Cao, G., Expanded Hydrated Vanadate for High-performance Aqueous Zinc-ion Batteries. *Energy Environ. Sci.* **2019,** *12* (7), 2273-2285.

2. Wang, D.; Wang, L.; Liang, G.; Li, H.; Liu, Z.; Tang, Z.; Liang, J.; Zhi, C., A Superior Delta-MnO_2 Cathode and a Self-Healing Zn-delta-MnO_2 Battery. *ACS Nano* **2019,** *13* (9), 10643-10652.